

Cerebellar granule cells acquire a widespread predictive feedback signal during motor learning

Andrea Giovannucci^{1,2,11}, Aleksandra Badura^{1,3,11}, Ben Deverett^{1,4}, Farzaneh Najafi^{5,10}, Talmo D Pereira¹, Zhenyu Gao⁶, Ilker Ozden^{1,7}, Alexander D Kloth^{1,10}, Eftychios Pnevmatikakis^{2,8}, Liam Paninski⁸, Chris I De Zeeuw^{3,6}, Javier F Medina⁹ & Samuel S-H Wang¹

Cerebellar granule cells, which constitute half the brain's neurons, supply Purkinje cells with contextual information necessary for motor learning, but how they encode this information is unknown. Here we show, using two-photon microscopy to track neural activity over multiple days of cerebellum-dependent eyeblink conditioning in mice, that granule cell populations acquire a dense representation of the anticipatory eyelid movement. Initially, granule cells responded to neutral visual and somatosensory stimuli as well as periorbital airpuffs used for training. As learning progressed, two-thirds of monitored granule cells acquired a conditional response whose timing matched or preceded the learned eyelid movements. Granule cell activity covaried trial by trial to form a redundant code. Many granule cells were also active during movements of nearby body structures. Thus, a predictive signal about the upcoming movement is widely available at the input stage of the cerebellar cortex, as required by forward models of cerebellar control.

The cerebellum is widely recognized as supporting associative learning necessary for generating predictive and corrective actions in specific contexts¹. Contextual information is thought to be encoded at the input level of the cerebellum in the granule cell (GrC) population² and may include peripheral and internally generated sensory signals^{1,3–5} as well as feedforward signals about a learned motor command^{6,7}. However, little is known about actual GrC representations during the learning process, because cerebellar learning is slow⁸ and single-cell recording methods only allow GrCs to be monitored on a single day for a brief period of time^{9–11}.

The question of how GrCs represent contextual information during behavior can be understood in terms of several models of cerebellar information processing. In one longstanding hypothesis, contextual information is provided by a very small fraction of GrCs, speculatively as few as ~1% (ref. 3). For associative learning during eyeblink conditioning, such subpopulations of GrCs have been suggested as representing externally generated conditional stimuli (CSs), such as tones or light flashes^{12,13}. The pairing of CSs with an unconditional stimulus (US), such as a corneal airpuff, triggers learning processes in which the resulting changes in CS-driven Purkinje cell spiking drive a well-timed blink that protects the eye—a conditional response (CR)^{12,13}.

In the domain of continuous actions such as smooth movements, it has also been suggested that the cerebellum conveys a broader range of information as part of a feedback system for control of overall brain

output^{14,15}. In forward models for motor control, it is suggested that the outcomes of actions are continually being predicted, with the prediction being fed back within the brain as part of a dynamic process of adjustment¹⁴. Such models require that GrC inputs to the cerebellum convey not only external-world information such as CSs but also internally generated predictions of action on an ongoing basis.

We tested these ideas about neural representations in GrCs by using two-photon microscopy of calcium indicator protein GCaMP6f to image populations of GrCs while mice underwent classical eyeblink conditioning in a head-fixed apparatus. This combination of methods allowed us to follow the evolution of learned GrC representations over many days.

RESULTS

Monitoring cerebellar GrC calcium signals in behaving mice

We expressed GCaMP6f or fast-GCaMP6f-RS09 in cerebellar lobule VI (Fig. 1a) using two adeno-associated virus type 1 (AAV1)-based strategies. In wild-type mice, we injected an AAV1 construct that used the human synapsin (hSyn) promoter to drive widespread expression in the GrC layer¹⁶. In NeuroD1-cre mice from the laboratory of M.E. Hatten, we used a conditional strategy by injecting AAV1-Flex-GCaMP6f. Both strategies led to widespread expression in the GrC layer (Fig. 1b and Supplementary Fig. 1). We selected for monitoring regions of interest (ROIs) that met criteria of near-circularity and diameters of 4.5–7.5 μm , often with an annular pattern of fluorescence. Positive

¹Princeton Neuroscience Institute and Department of Molecular Biology, Princeton University, Princeton, New Jersey, USA. ²Center for Computational Biology, Flatiron Institute, Simons Foundation, New York, New York, USA. ³Netherlands Institute for Neuroscience, Amsterdam, the Netherlands. ⁴Robert Wood Johnson Medical School, New Brunswick, New Jersey, USA. ⁵Department of Biology, University of Pennsylvania, Philadelphia, Pennsylvania, USA. ⁶Department of Neuroscience, Erasmus MC, Rotterdam, the Netherlands. ⁷School of Engineering, Brown University, Providence, Rhode Island, USA. ⁸Departments of Statistics and Neuroscience, Columbia University, New York, New York, USA. ⁹Department of Neuroscience, Baylor College of Medicine, Houston, Texas, USA. ¹⁰Present addresses: Cold Spring Harbor Laboratory, Cold Spring Harbor, New York, USA (F.N.) and University of North Carolina, Chapel Hill, North Carolina, USA (A.D.K.). ¹¹These authors contributed equally to this work. Correspondence should be addressed to S.S.-H.W. (sswang@princeton.edu) or J.F.M. (jmedina@bcm.edu).

Received 8 November 2016; accepted 17 February 2017; published online 20 March 2017; doi:10.1038/nn.4531

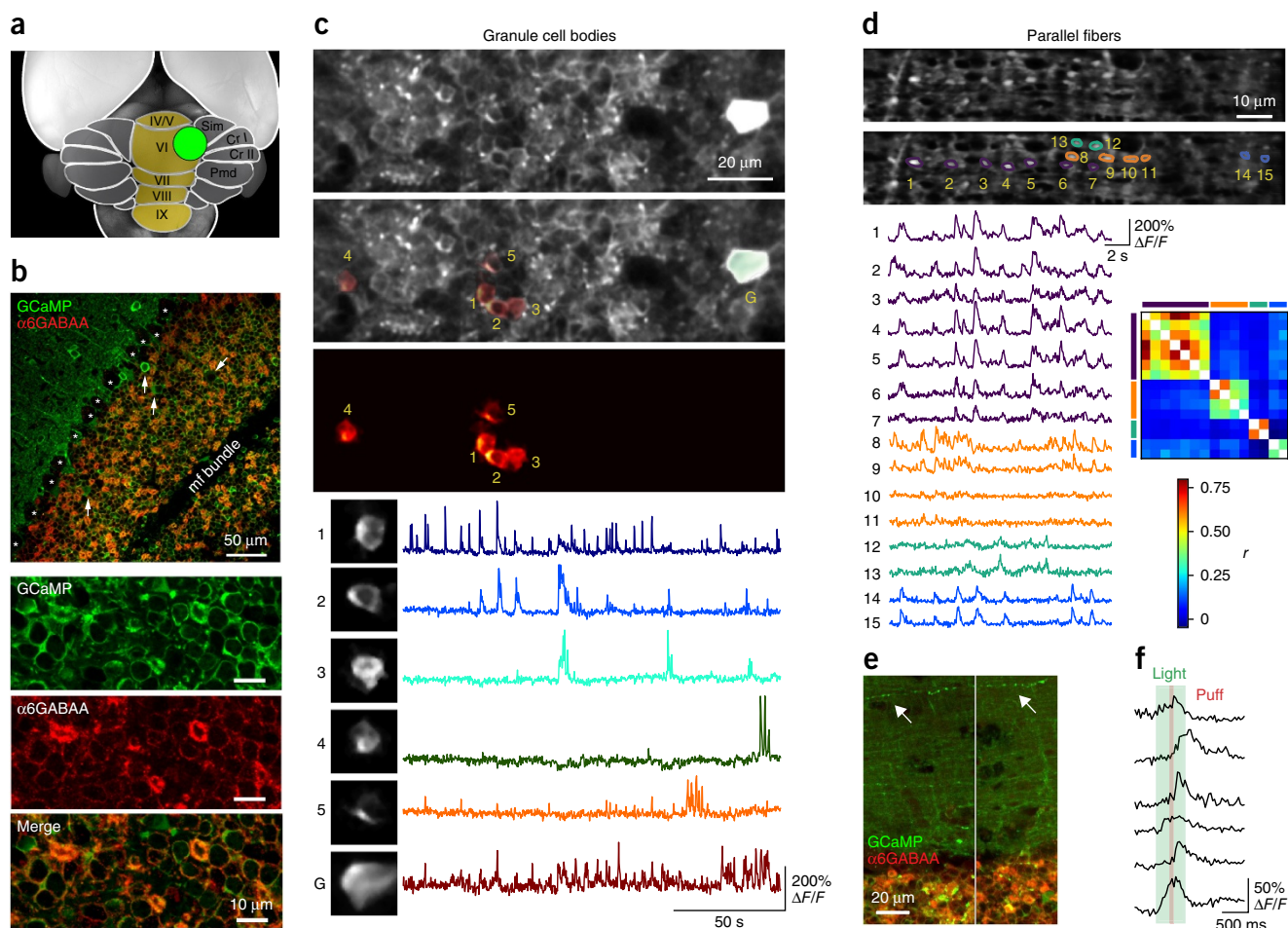


Figure 1 GCaMP expression and signals in cerebellar GrCs. (a) Dorsal view of the cerebellum with imaged area of lobule VI indicated in green. (b) GABA_A α6 staining (red) highlights dense virally driven expression of GCaMP6f (green) in GrCs (GrCs; each FOV of 100 × 100 μm contained an average of 187 GrCs; 20 FOVs and 2 mice per expression strategy, NeuroD1-cre and hSyn). Note the absence of GCaMP signal in the mossy fiber (mf) bundle and Purkinje cells (asterisks). Arrows indicate putative Golgi or Lugaro cells. (c) Top: three panels show (from top to bottom) two-photon imaging FOV in the granular layer, overlaid with a subset of spatial components identified by NMF and classified as GrCs (red) or a putative Golgi cell (green, G) and the same GrCs on a dark background. Bottom: GrC fluorescence traces and corresponding spatial mask. (d) Two-photon imaging of parallel fiber activity. Top: an example FOV without and with manually selected regions of interest. Bottom left: fluorescence traces. Bottom right: cross-correlations reveal high correlation between mediolaterally aligned boutons. (e) Coronal cerebellar sections of the mouse shown in d, counterstained for GABA_A α6. Arrows point to a parallel fiber expressing GCaMP6f. (f) Fluorescent traces from parallel fiber boutons recorded from a trained mouse, aligned to corneal airpuffs and light flashes.

staining for the GrC-specific GABA_A α6 subunit was found in 99.7 ± 0.1% of such ROIs in both hSyn-injected (wild-type) and NeuroD1-cre mice, indicating that virtually all monitored structures belonged to GrCs. We also found that 94 ± 2% of all ROIs were DAPI-positive at the center, completing their identification as GrC somata. No mossy fiber-like structures were observed to express GCaMP. As indicated by the pattern of nonexpressing voids (Fig. 1b), no Purkinje cells were seen; in the case of the synapsin promoter, this was consistent with previous results^{17,18}. Larger, DAPI-positive and α6-negative structures were occasionally observed and tentatively classified as Golgi or Lugaro cells (Fig. 1b and Supplementary Fig. 1). Thus, our *in vivo* imaging criteria predominantly identify individual GrC somata (Fig. 1c).

In two NeuroD1-cre mice, we further confirmed GrC expression by imaging at molecular-layer locations. We observed axon-like structures and boutons (Fig. 1d,e). These structures were active in the absence of any applied stimuli and responded to corneal airpuffs and light flashes (Fig. 1f and Supplementary Video 1). Signals from rows of mediolaterally aligned boutons were strongly correlated

(Fig. 1d), consistent with a common origin from shared parallel fibers and indicative of the propagation of action potentials.

In brain slices, we measured GrC somatic fluorescence signals while evoking and monitoring action potentials electrically via mossy fiber stimulation or patch electrode (Supplementary Fig. 2). We recorded action potentials in cell-attached mode to prevent GCaMP wash-out, which occurs during whole-cell recording. Fluorescence signal amplitude increased monotonically as a function of the number of mossy fiber stimuli (Supplementary Fig. 2a,b) and as a function of action potentials, up to the highest number of spikes tested, 20 spikes at 50–600 Hz (Supplementary Fig. 2c). In published observations of *in vivo* GrC activity recorded during awake behavior, including locomotion¹⁰ and whisker stimulation¹¹, brief high-frequency bursts have been observed (10–14 spikes at 40–170 Hz (ref. 10) and 1–25 spikes at 270–440 Hz (ref. 11), respectively). In this range of activity in brain slices, we found that the fluorescence increase ranged from $\Delta F/F_0 = 24\%$ to 155% (Supplementary Fig. 2c). In our experiments, *in vivo* calcium imaging of 268 GrCs whose activity was highly

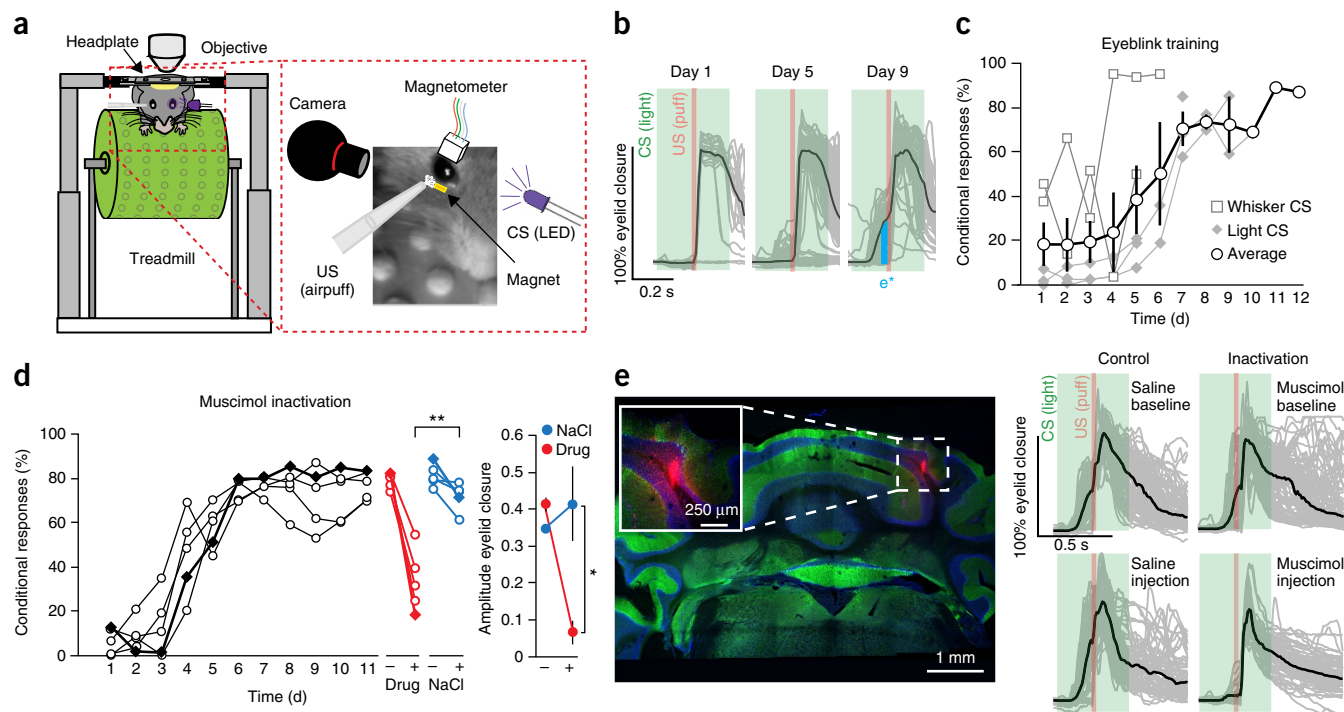


Figure 2 Role of imaged regions in eyeblink conditioning. **(a)** Task schematic. CS (ultraviolet LED flash to the contralateral eye or weak puff to the ipsilateral vibrissa) and US (periorbital airpuff) were delivered to a head-fixed mouse on a freely moving treadmill while blinks, snout movement, body movement and treadmill rotation were monitored by high-speed infrared camera (100 frames/s) and (in some experiments) a magnet attached to the lower eyelid. **(b)** CRs, quantified as eyelid closure as a fraction of US response, during CS–US paired trials in a single animal. Green (CS, light) and red (US, airpuff) shaded zones indicate stimulus presentations. Blue shaded zone indicates time window for computing e^* , eyelid movement as a measure of CR amplitude. **(c)** Evolution of learning in 6 animals trained for up to 12 consecutive d (2 mice trained with whisker CS, open squares; 4 mice trained with light CS, closed gray diamonds; average indicated by open circles). Error bars for the averaged plot indicate \pm s.e.m. **(d)** Left: focal injection of muscimol, but not saline vehicle, led to a reduction in the percentage of CRs (muscimol (drug) versus saline CR probability, $P = 0.005$, paired t -test; each line represents one animal). Filled symbols depict data for the example mouse shown in **e**. Right: focal injection of muscimol, but not saline vehicle, led to a reduction in the amplitude of CRs (muscimol versus saline CR, $P = 0.026$, paired t -test; $n = 5$). Blue and red dots depict averages. Error bars indicate \pm s.e.m. **(e)** Example of the inactivation experiment in one mouse (filled diamonds in **d**, left). Left: a coronal cerebellar section counterstained with DAPI (blue) and aldolase C (green) reveals the injection position (red, muscimol + Evans Blue). Right: individual (light gray) and averaged (black) eyelid responses during baseline trials before injections and after drug or saline injections.

correlated with locomotion ($r > 0.6$; $n = 5$ mice) revealed $\Delta F/F_0$ signals ranging from 23% to 165%. Thus GCaMP signals *in vivo* were consistent with expectations from published electrophysiological observations of GrC activity.

Chronic *in vivo* imaging of cerebellar cortex during eyeblink conditioning

For *in vivo* imaging (Supplementary Video 2) of learned representations, we followed 128 GrCs for up to 12 d of training in 3 mice in the same 3 fields of view (FOVs; Supplementary Fig. 3) and 268 \pm 91 GrCs in FOVs reimaged over one or more sessions without one-to-one cell matching in 3 additional mice (98 FOVs). To investigate GrC representations, we used classical eyeblink conditioning (Fig. 2a), a form of Pavlovian learning that requires cerebellar activity and plasticity^{13,19}. Mice were trained by pairing a CS in the form of a flash of light ($n = 4$) or a weak airpuff to the ipsilateral whisker area ($n = 2$) with an aversive US, a periorbital airpuff, which reliably evoked an unconditional reflex blink (UR; Fig. 2b). After repeated pairings of the CS and US over the course of multiple conditioning sessions, the CS alone came to elicit an anticipatory eyeblink CR that started before the time of the expected US onset and was part of a broader avoidance response²⁰. By the end of training, CRs were elicited on an average

of $73 \pm 13\%$ (range 58–96%) of all trials and CR amplitude reached $43 \pm 7\%$ of the US-triggered full eyelid closure (Fig. 2c).

In all mice ($n = 6$), we imaged GrCs near the surface of cerebellar lobule VI (Fig. 1a), an optically accessible region that, although not previously included among known regions necessary for the production of blinks^{21–23}, receives excitation that drives movements of nearby trunk and neck regions (Supplementary Fig. 4) and is likely to be engaged during eyeblink conditioning because it receives climbing fiber inputs triggered by the periorbital airpuff US^{24,25}. Indeed, in separate nonimaging experiments with five mice that were trained to a high fraction of conditional responses (CR rate $> 70\%$), we found that injection of muscimol in the same region of cerebellar cortex led to a reversible reduction in CR probability and amplitude (Fig. 2d,e). CR probability decreased from $81\% \pm 5\%$ (mean \pm s.d.) during the baseline measurements to $39\% \pm 19\%$ (Fig. 2d), an effect that was not seen after control injections of saline in the same animals ($72\% \pm 6\%$; different from muscimol injection, $P = 0.005$; CR amplitude smaller in muscimol condition than saline injection, $P = 0.026$; Fig. 2d). The degree of impairment caused by muscimol increased with the size of the injected area within the anterior-lateral lobule VI (Supplementary Fig. 5) indicating that this region played a significant role in modulating the production of learned blinks.

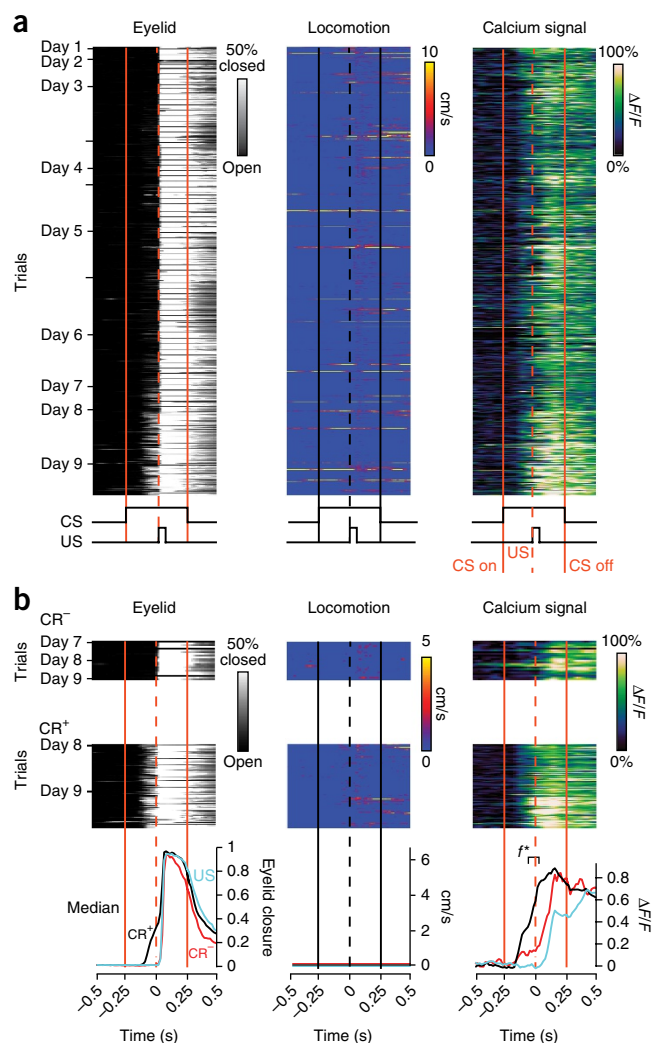


Figure 3 Calcium signals of a single GrC during eyeblink conditioning. (a) Eyelid movement (left), locomotion activity (center) and single-cell calcium signal (right) from one neuron followed over 9 d of training. Each horizontal line represents a single trial. Date labels indicate the start of a day's training, and unlabeled ticks indicate the start of a new session within the same day. Vertical solid lines indicate onset and offset of CS stimulus. Dashed vertical lines indicate delivery time of the US stimulus. (b) Top: data from the last 3 d of training, resorted according to whether the CS did (CR⁺, middle) or did not (CR⁻, top) evoke an anticipatory eyelid closure before the US. Trials with significant locomotion (> 2 cm/s) during the CS are excluded. Bottom left: overlaid average eyelid responses in US trials (cyan) and at the final stage of training when the animal did (CR⁺, black) or did not (CR⁻, red) produce a CR. Bottom middle: overlaid average locomotion speeds during US, CR⁺ and CR⁻ trials. Bottom right: overlaid average calcium signals during US, CR⁺ and CR⁻ trials. f^* is the integral of the neural response in an 85-ms window before the UR.

Figure 3 shows trial-by-trial recordings of calcium signals in a single GrC, along with simultaneously recorded behavioral responses over the course of 9 d of conditioning using a CS (Fig. 3a and Supplementary Fig. 6). To demix and denoise somatic signals from the surrounding neuropil, we used structured matrix factorization methods²⁶ (Supplementary Video 2). In addition to measuring eyelid closure (Fig. 3a,b), we used computer-assisted analysis of video recordings to calculate treadmill speed (Fig. 3a,b) and combined whisker-and-snout movement (Supplementary Fig. 7 and

Supplementary Videos 3 and 4). These algorithms allowed us to resolve movements with single-frame resolution.

GrCs develop a trial-by-trial representation of the learned response

To assess the relationship between behavioral and cellular responses, we divided all data into trials in which only the periorbital puff was delivered (US), trials in which the animal produced no CR and showed no significant locomotion (speed < 2 cm/s) during the CS presentation (CR⁻; Fig. 3b), and trials in which the mouse produced a CR but showed no significant locomotion (speed < 2 cm/s) during the CS presentation (CR⁺; Fig. 3b). Trials with snout/whisker movements were kept because these are part of the CR^{8,20}. The example neuron highlights three features of GrC responses. First, the US evoked a large calcium response in all trials (Fig. 3b and Supplementary Fig. 6). This response was consistent with drive either from activation of somatosensory inputs from the periorbital area or from motor signals linked to the reflex blink or high levels of movement. Second, presentation of the CS evoked a smaller calcium response detectable even on trials with no CR and no significant locomotion (Fig. 3b), suggesting that it could have been driven either by sensory inputs or by undetected movements. Third, individual GrC responses were substantially larger on CR⁺ trials than on CR⁻ trials (Fig. 3b and Supplementary Fig. 6b), an effect that could be explained by activation of CR-related inputs. Thus, this example GrC was active during eyeblink conditioning and carried a signal correlated with the presence or absence of the CR.

GrCs acquire a predictive control signal

If GrC calcium signals were related to CRs, they would be expected to have temporal dynamics that matched the eyelid response and to grow in amplitude with learning (Fig. 4). For both light CS and whisker CS (Fig. 4a), the GrC population activity preceded the onset of the eyelid response on average (Supplementary Fig. 8a,b). In GrCs with a correlation with CR amplitude > 0.3 , the signal preceded the start of eyelid closure by 68 ± 28 ms and the start of the snout or whisker movement by 142 ± 33 ms (185 neurons, 4 mice; Supplementary Fig. 8b), consistent with a predictive control signal and ruling out sensory reafference as the sole mechanism.

To test whether GrC responses grew with learning, we examined calcium responses and behavioral output across training days (Fig. 4). We quantified the magnitude of eyelid movement (Fig. 4a) and GrC calcium response (f^*) in CR⁺ and CR⁻ trials in an 85-ms time window preceding the UR. Figure 4b shows how calcium signals evolved over the course of 9 d of conditioning for one FOV comprising 29 GrCs. In individual GrCs (Fig. 4b), CR⁺-associated calcium responses grew with training while CR⁻-associated responses did not. Calcium signals in CR⁺ trials increased in parallel with eyelid closure amplitude (Fig. 4b), while overall average animal locomotion was below 0.05 cm/s (Fig. 4b). We obtained similar results in all the other FOVs ($n = 6$ mice), after accommodating for the learning dynamics of the different animals by binning GrC activity according to the level of performance (Fig. 4c). Thus, across the population of GrCs, the average f^* increased progressively for low-, medium- and high-probability CR epochs (Fig. 4c and Supplementary Fig. 8c; left: Pearson's $r = 0.21 \pm 0.04$, $P = 1.8 \cdot 10^{-6}$; right: $r = 0.12 \pm 0.04$, $P = 0.004$; mean \pm s.d. from bootstrapping procedure), indicating that learning was accompanied by the emergence of a CR-specific GrC signal.

GrC representations are dense on a subsecond time scale

Analysis of calcium responses in populations of GrCs revealed that most GrCs were activated by the CS in CR⁻ trials (Fig. 4d and

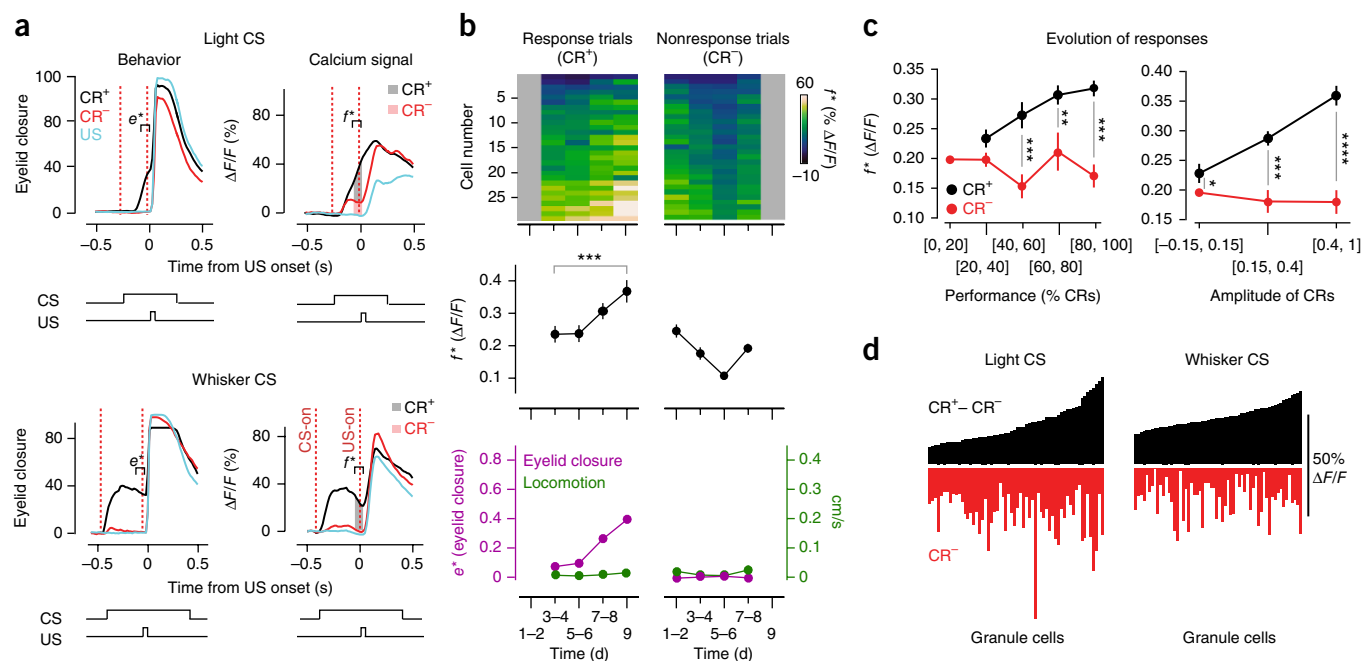


Figure 4 Cerebellar GrCs acquire a neural correlate of the learned conditional response. **(a)** Top: in a mouse trained with light CS, average CR amplitude (first column) and fluorescence responses (second column) for populations of GrCs grouped by trial type ($n = 29$ neurons). US, cyan; CR⁺ trials, black; CR⁻ trials, red. Bottom: same results for a mouse trained with whisker CS ($N = 60$ neurons). Behavioral and neural traces averaged over an 85-ms time window (brackets) preceding the UR for eyelid responses (e^*) and fluorescence response (f^*). Shaded regions in the right column represent the amount of GrC response in CR⁻ trials (red) and the excess GrC response in CR⁺ vs. CR⁻ trials (black). **(b)** Top: evolution of the calcium response during 9 d of conditioning to a CS light stimulus, shown separately for CR⁺ (left) and CR⁻ (right) trials in 29 individual GrCs from a single animal. Gray indicates that not enough trials (5) were available to compute a value. Middle: average calcium responses for the 29 GrCs in the population as a function of training day. Responses before and after training were significantly different (paired t -test, $P = 5.7 \times 10^{-7}$). Bottom: eyelid response and locomotion for CR⁺ and CR⁻ trials. Error bars indicate \pm s.e.m. **(c)** Evolution of GrC calcium responses across all animals ($n = 6$). Plotted values show average \pm s.e.m. calculated by bootstrap-resampling ($n = 480$ neurons, eyelid-amplitude CR⁺ trials; $n = 1,120$ cells, eyelid-amplitude CR⁻ trials; $n = 459$ neurons, percentage responses CR⁺ trials; $n = 1,109$ neurons, percentage responses CR⁻ trials) to obtain equal weighting among FOVs across 6 mice. Left: 0–20%, 20–40%, 40–60%, 60–80% and 80–100% of CRs. Right: blocks of trials sorted by e^* . For the significant bins, from left to right, t -tests: CR⁺ vs. CR⁻, $P = 2.5 \times 10^{-4}$, 7.8×10^{-3} and 6.1×10^{-4} (left), and $P = 0.041$ and 1.6×10^{-4} , 0.81×10^{-6} (right). Error bars indicate \pm s.e.m. * $P < 0.05$; ** $P < 0.01$; *** $P < 0.001$; **** $P < 0.0001$. **(d)** Histograms of GrC responses in 2 fully trained mice (one trained with whisker CS and one with light CS; for other mice see Supplementary Fig. 8d). Each histogram bar represents the response of a single GrC to a CS stimulus without wheel movement. Red histograms, $\Delta F/F$ for trials with no conditional response (CR⁻, same time bin as f^*); black histograms, difference in $\Delta F/F$ between CR⁺ and CR⁻ trial responses for the same cells, i.e., the CR⁺ excess (same time bin as f^*); $n = 60$ cells, light CS; $n = 60$ cells, whisker CS.

Supplementary Fig. 8d; 1 FOV per mouse), and they also carried a CR-related signal (defined as the difference in the f^* signal between CR⁺ and CR⁻ trials; Fig. 4d and Supplementary Fig. 8d). In fact, when we inspected individual GrCs across all FOVs in all mice ($n = 6$) we found that most of them ($64 \pm 18\%$) carried a signal that was CR-related (i.e., the trial-by-trial activity was significantly correlated with the eyelid response; see Online Methods).

Our custom matrix factorization algorithm²⁶ recognized 58 ± 18 GrCs per $10,000 \mu\text{m}^2$. Based on a total density of 187 ± 27 GrCs per $10,000 \mu\text{m}^2$ as determined by histological analysis, this corresponds to an estimated $31 \pm 10\%$ of all GrCs. Thus, at a minimum, $0.64 \times 31\% = 21\%$ of all GrCs within the FOV encoded CR-related contextual information during the CS period.

Because optogenetic activation of mossy fibers innervating the imaged area of lobule VI resulted in neck, trunk and limb movements (Supplementary Fig. 4), we surmised that GrC activity in this region might be associated with actions other than the production of learned blinks. Indeed, we found GrCs with calcium signals that were correlated with eyelid movement, wheel speed or snout movement (Fig. 5a). We quantified these correlations computing the Pearson's r coefficient between the GrC signals and behavior (Fig. 5b,c). In addition, some individual GrCs showed activity that correlated

with multiple movement parameters (Fig. 5d). To categorize each GrC according to its preferred movement parameter, we identified the one movement (eyelid-CR, snout, wheel or eyelid-UR) that was most highly correlated with its calcium signal. In animals that reached the advanced stage of training and with behavioral data available ($> 60\%$ conditional responses, $n = 3$ mice), more GrCs were best correlated with eyelid-CR than with any of the other movements (Fig. 5e).

Redundant coding of the learned response

The strong correlation between calcium signals and behavior in many individual GrCs suggests that the code may be redundant at the level of the population. To test for redundancy in GrC representations, we used the previously computed Pearson's correlation values for eyelid-CR to calculate the degree to which individual and multiple GrCs could encode a well-quantified movement parameter, CR amplitude. A linear regressor based on the activity of all the GrCs in the population was more correlated with CR amplitude than any single GrC (Fig. 6a), indicating that the CR was more accurately encoded by a distributed representation of GrC activity.

We quantified the degree of redundancy across the GrC population by computing the regressor's capacity to predict CR amplitude trial by trial. Capacity was measured in units of Shannon mutual information

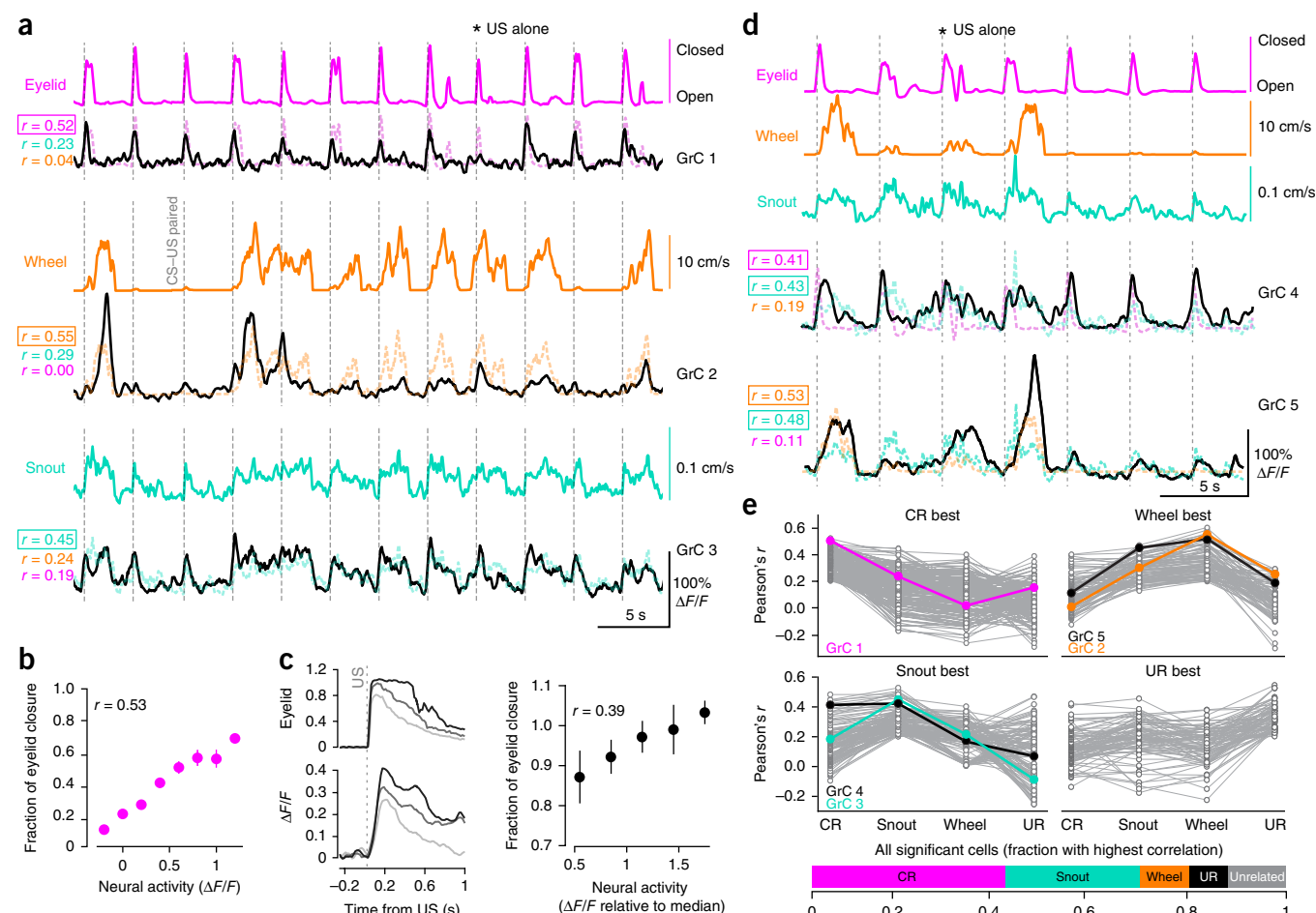


Figure 5 GrCs simultaneously express correlates of eyeblink, locomotion and snout movement. **(a)** Simultaneous recording of three GrCs whose calcium signals (black) were correlated with eyelid (magenta), wheel (orange) or snout (cyan) movements. Pearson correlations over one day's recording session are given in the left column. Dashed traces superimposed on the calcium signals are the same movement-related traces shown in the panels above. **(b)** In a single GrC, eyelid responses to CS presentation (e^*) as a function of fluorescence signal (f^*). Error bars indicate \pm s.e.m. **(c)** Left: in a single GrC, US-only presentation caused a range of eyelid response amplitudes (URs) concurrent with changes in f^* . Right: eyelid closure amplitude as a function of neural activity in a single GrC, averaged across US-only trials. **(d)** Examples of GrCs with high correlations to two behavioral parameters. **(e)** In three mice with the strongest learning and a high CR rate, tuning of all imaged GrCs (gray lines and open circles) to eyelid CR, snout movement, wheel speed and eyelid UR amplitude. Tunings corresponding to the GrCs in **a** (colored lines and circles) and **d** (black lines and circles) are highlighted. Bottom: the distribution of GrCs with strongest correlation to each individual behavior. Asterisks indicate US-alone trials.

between the regressor output and the eyelid trace. Mutual information increased with the number of neurons included in the regressor (**Fig. 6b**) but rapidly reached a plateau as more neurons were added. The amount of redundancy in the GrC population was calculated using a redundancy index, Λ , which was defined as the upper bound of information contained in the neurons individually, divided by the amount of information contained in the population regressor. Under this definition of redundancy, when $\Lambda = 1$, each GrC provides independent information. When all imaged neurons were included, the median value of Λ was 12 (range, 7 to 140; $n = 6$ mice), exceeding levels seen elsewhere in the central nervous system^{27,28}. Λ increased proportionally with the number of GrCs monitored ($r = +0.89$), and since many active GrCs were not imaged in our experiments, the true degree of redundancy is likely to be even higher.

DISCUSSION

Our findings demonstrate that neural activity related to learned movements was available at the input stage of cerebellar cortex and in a notably high fraction of GrCs. This signal may arise from cells

in the anterior interpositus nucleus that increase their firing during the CR^{8,13,29}. Deep nuclear activity can lead to net excitation of GrCs by two routes: monosynaptic excitation, via collaterals of principal cells that terminate as mossy fibers^{7,30}, and disinaptic disinhibition, via inhibitory deep nuclear neuron projections onto Golgi cells, which in turn inhibit GrCs³¹. Descending action-related information may also arrive in the cerebellum via corticopontine pathways, which can converge onto the same GrCs as sensory pathways⁶. It has been suggested that the cerebellum may use signals like those we have uncovered as a form of efference copy to compute forward models that overcome the problems associated with long delays in sensory feedback^{14,15}. In this way, the duality between driving behavioral output and receiving a copy of the output may allow the cerebellum to participate in a closed feedback loop that regulates and adjusts ongoing predictive responses in real time¹⁵.

Single GrCs were activated during multiple distinct movements with specificity that was often, but not always, restricted to eyelid, snout or locomotion. These correlations described a representation of both unconditional and conditional movement and are

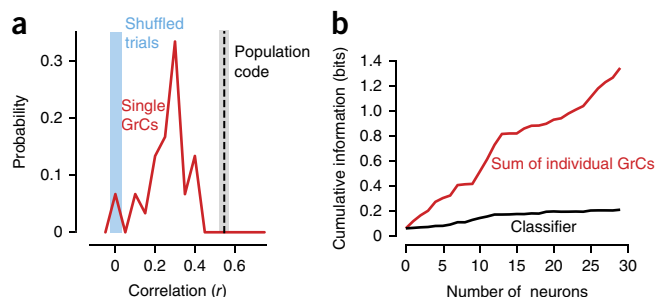


Figure 6 Redundancy in the GrC representation of learned responses. (a) For one example mouse, a histogram of Pearson correlations for all neurons (red, values larger than the shuffled range shown). The black dashed line indicates the Pearson correlation between the output of the population multivariate regressor and the actual eyelid response (e^*) for multiple runs. Gray shading indicates the ± 1 s.d. range of regressor performance. The cyan band indicates the correlations for single cells when the eyelid responses in individual trials are randomly shuffled. (b) Information content of the population regressor (black) as a function of the number of neurons included. The red curve indicates the maximum possible information in the case of no redundancy.

consistent with the idea that the mossy fiber pathway in this region of lobule VI provides a stream of information that is available for the generation and control of movements by separate but nearby body structures³².

Dense coding: beyond the theories of Marr and Albus

Traditional theories of cerebellar function^{3,4} emphasize that the pattern of connectivity and the staggering number of GrCs in the cerebellar cortex makes these cells perfectly suited to produce high-dimensional representations, in which each context is encoded by a unique pattern of activity in the GrC population and a slight change in context strongly alters the pattern of activity. The theories of Marr and Albus suggest that (i) individual cells should fire only rarely and (ii) the activity of GrCs should be uncorrelated³². Until now, these predictions have not been tested directly because it was not technically possible to monitor activity in a population of GrCs during cerebellum-dependent tasks. Our evidence did not match these classical predictions. Instead, we observed contextual, redundant activity, consistent with a dense representation³².

Any distinction between the concepts of 'sparse' and 'dense' encounters the difficulty that a wide range of activity is often considered to be sparse, as long as "low levels of firing [occur] under some circumstances"⁴. We found that during the CS period, approximately two-thirds of imaged GrCs were active. This fraction is far from Albus's original speculation, in which he suggested that an entire sensory context would be coded by a tiny fraction of GrCs: "if this density ... is 1% or less, patterns are easily recognized and quickly learned." The fraction of granule cells active in the CS period appears significantly larger than predicted by Marr as well (p. 469 of ref. 3): "the number of GrCs active at any one time (say in any 50 msec period) is a small fraction (less than 1/20) of all granule cells". However, these comparisons are fair only if the interval of comparison is an entire action, i.e., the CR taken as a whole. GrC activity could transmit information on a finer time scale, as would occur if the CR were regulated dynamically in time, for instance, using a forward model. In a sense, whether the patterns we observed can be considered dense depends on how closely in time GrCs must fire in order to be considered simultaneously active. Future methods for monitoring activity with higher time resolution may help answer the sparse-versus-dense question.

Dynamic regulation of behavior by efference copy

We found that, by the end of training, GrC responses were strongly dependent on whether a CR was produced. The population response contained temporal components that both preceded and occurred simultaneously with the motor command. This brings up the possibility that GrC populations act as a source of behavioral variation. Previously, it has been found that the firing rate of individual Purkinje cells is highly correlated with learned movements on a trial-by-trial basis^{33,34}, suggesting that the firing of entire Purkinje cell populations must be highly correlated. Our finding of population-level covariation in GrC firing suggests that, in the production of cerebellar-driven movements, Purkinje cell populations could derive their correlation from the fact that they receive input signals that are themselves highly correlated³⁵.

Since inhibition of the imaged locations leads to disruptions in learned blink amplitude, the observed learning-related neural responses in GrCs may drive Purkinje cell responses, whose firing carries a neural correlate of the CR (ref. 36). Lobule VI and its neighboring regions in simplex lobule and anterior vermis contribute to eyeblink conditioning, autonomic responses that accompany conditioning²⁰, and neck, trunk and forelimb defensive movements^{21,37}. In such a cerebellar region capable of forming multiple, related associations, redundancy might help the system amplify its learned blink response³⁰ as well as increase its ability to discriminate between³⁸, and generalize to, new stimuli⁵. In this way, a copy of the learned output may help the cerebellum to refine an action as brief as an eyeblink dynamically while it is being produced.

METHODS

Methods, including statements of data availability and any associated accession codes and references, are available in the [online version of the paper](#).

Note: Any Supplementary Information and Source Data files are available in the online version of the paper.

ACKNOWLEDGMENTS

The authors thank L. Lynch for expert laboratory assistance, A.C.H.G. Ijpelaar for technical assistance and Dr. H. Boele of the Neuroscience department at the Erasmus Medical Center for their input in eyeblink recordings, M.J. Berry II for discussion of the information calculation, D. Dombeck, J.P. Rickgauer and C. Domnisoru for experimental advice, and D. Pacheco-Pinedo, J.L. Verpeut, P. Sanchez-Jauregui and I. Witten for comments and suggestions. This work was supported by National Institutes of Health grants R01 NS045193 (S.W.) and R01 MH093727 (J.M.), New Jersey Council on Brain Injury Research fellowship CBIR12FEL031 (A.G.), the Searle Scholars program (J.M.), DARPA N66001-15-C-4032 (L.P.), National Science Foundation Graduate Research Fellowship DGE-1148900 (T.P.), the Nancy Lurie Marks Family Foundation (S.W.), the Netherlands Organization for Scientific Research (Innovational Research Incentives Scheme Veni; A.B. and Z.G.), the Dutch Fundamental Organization for Medical Sciences (ZonMW; C.I.D.Z.), Life Sciences (NWO-ALW; C.I.D.Z.) and Social and Behavioral Sciences (NWO-MAGW; C.I.D.Z.), as well as ERC-adv and ERC-POC (C.I.D.Z.).

AUTHOR CONTRIBUTIONS

A.G. designed behavioral and imaging experiments, established the behavioral and imaging setup and molecular methods, performed *in vivo* imaging experiments, developed analyses and drafted the manuscript. A.B., Z.G. and C.I.D.Z. designed and/or performed brain slice experiments. A.B. performed histological and combined behavioral-pharmacological experiments. F.N., I.O., B.D. and A.D.K. established the behavioral and imaging setup and methods. B.D. performed *in vivo* imaging experiments and developed analyses. T.D.P., E.P. and L.P. developed analyses. J.F.M. and S.S.-H.W. designed experiments and developed analyses. All authors edited the manuscript.

COMPETING FINANCIAL INTERESTS

The authors declare no competing financial interests.

Reprints and permissions information is available online at <http://www.nature.com/reprints/index.html>.

1. Ito, M. Cerebellar circuitry as a neuronal machine. *Prog. Neurobiol.* **78**, 272–303 (2006).
2. Arenz, A., Bracey, E.F. & Margrie, T.W. Sensory representations in cerebellar granule cells. *Curr. Opin. Neurobiol.* **19**, 445–451 (2009).
3. Marr, D. A theory of cerebellar cortex. *J. Physiol. (Lond.)* **202**, 437–470 (1969).
4. Albus, J.S. A theory of cerebellar function. *Math. Biosci.* **10**, 25–61 (1971).
5. Spanne, A. & Jörntell, H. Questioning the role of sparse coding in the brain. *Trends Neurosci.* **38**, 417–427 (2015).
6. Huang, C.C. *et al.* Convergence of pontine and proprioceptive streams onto multimodal cerebellar granule cells. *Elife* **2**, e00400 (2013).
7. Houck, B.D. & Person, A.L. Cerebellar premotor output neurons collateralize to innervate the cerebellar cortex. *J. Comp. Neurol.* **523**, 2254–2271 (2015).
8. Heiney, S.A., Wohl, M.P., Chetthi, S.N., Ruffolo, L.I. & Medina, J.F. Cerebellar-dependent expression of motor learning during eyeblink conditioning in head-fixed mice. *J. Neurosci.* **34**, 14845–14853 (2014).
9. Eccles, J.C., Faber, D.S., Murphy, J.T., Sabah, N.H. & Táboriková, H. Afferent volleys in limb nerves influencing impulse discharges in cerebellar cortex. I. In mossy fibers and granule cells. *Exp. Brain Res.* **13**, 15–35 (1971).
10. Powell, K., Mathy, A., Duguid, I. & Häusser, M. Synaptic representation of locomotion in single cerebellar granule cells. *Elife* **4**, e07290 (2015).
11. van Beugen, B.J., Gao, Z., Boele, H.J., Hoebeek, F. & De Zeeuw, C.I. High frequency burst firing of granule cells ensures transmission at the parallel fiber to Purkinje cell synapse at the cost of temporal coding. *Front. Neural Circuits* **7**, 95 (2013).
12. Medina, J.F. & Mauk, M.D. Computer simulation of cerebellar information processing. *Nat. Neurosci.* **3** (Suppl.), 1205–1211 (2000).
13. Freeman, J.H. & Steinmetz, A.B. Neural circuitry and plasticity mechanisms underlying delay eyeblink conditioning. *Learn. Mem.* **18**, 666–677 (2011).
14. Shadmehr, R., Smith, M.A. & Krakauer, J.W. Error correction, sensory prediction, and adaptation in motor control. *Annual Rev. Neurosci.* **33**, 89–108 (2010).
15. Wolpert, D.M., Miall, R.C. & Kawato, M. Internal models in the cerebellum. *Trends Cogn. Sci.* **2**, 338–347 (1998).
16. Ozden, I., Dombeck, D.A., Hoogland, T.M., Tank, D.W. & Wang, S.S.-H. Widespread state-dependent shifts in cerebellar activity in locomoting mice. *PLoS One* **7**, e42650 (2012).
17. Kuhn, B., Ozden, I., Lampi, Y., Hasan, M.T. & Wang, S.S.-H. An amplified promoter system for targeted expression of calcium indicator proteins in the cerebellar cortex. *Front. Neural Circuits* **6**, 49 (2012).
18. Yaguchi, M. *et al.* Characterization of the properties of seven promoters in the motor cortex of rats and monkeys after lentiviral vector-mediated gene transfer. *Hum. Gene Ther. Methods* **24**, 333–344 (2013).
19. Boele, H.-J., Koekkoek, S.K.E. & De Zeeuw, C.I. Cerebellar and extracerebellar involvement in mouse eyeblink conditioning: the ACDC model. *Front. Cell. Neurosci.* **3**, 19 (2010).
20. Thompson, R.F. & Krupa, D.J. Organization of memory traces in the mammalian brain. *Annu. Rev. Neurosci.* **17**, 519–549 (1994).
21. Heiney, S.A., Kim, J., Augustine, G.J. & Medina, J.F. Precise control of movement kinematics by optogenetic inhibition of Purkinje cell activity. *J. Neurosci.* **34**, 2321–2330 (2014).
22. Hesslow, G. Correspondence between climbing fibre input and motor output in eyeblink-related areas in cat cerebellar cortex. *J. Physiol. (Lond.)* **476**, 229–244 (1994).
23. Mostofi, A., Holtzman, T., Grout, A.S., Yeo, C.H. & Edgley, S.A. Electrophysiological localization of eyeblink-related microzones in rabbit cerebellar cortex. *J. Neurosci.* **30**, 8920–8934 (2010).
24. Najafi, F., Giovannucci, A., Wang, S.S.-H. & Medina, J.F. Sensory-driven enhancement of calcium signals in individual Purkinje cell dendrites of awake mice. *Cell Rep.* **6**, 792–798 (2014).
25. Najafi, F., Giovannucci, A., Wang, S.S.-H. & Medina, J.F. Coding of stimulus strength via analog calcium signals in Purkinje cell dendrites of awake mice. *Elife* **3**, e03663 (2014).
26. Pnevmatikakis, E.A. *et al.* Simultaneous denoising, deconvolution, and demixing of calcium imaging data. *Neuron* **89**, 285–299 (2016).
27. Narayanan, N.S., Kimchi, E.Y. & Laubach, M. Redundancy and synergy of neuronal ensembles in motor cortex. *J. Neurosci.* **25**, 4207–4216 (2005).
28. Puchalla, J.L., Schneidman, E., Harris, R.A. & Berry, M.J. Redundancy in the population code of the retina. *Neuron* **46**, 493–504 (2005).
29. Freeman, J.H. Cerebellar learning mechanisms. *Brain Res.* **1621**, 260–269 (2015).
30. Gao, Z. *et al.* Excitatory cerebellar nucleocortical circuit provides internal amplification during associative conditioning. *Neuron* **89**, 645–657 (2016).
31. Ankri, L. *et al.* A novel inhibitory nucleo-cortical circuit controls cerebellar Golgi cell activity. *Elife* **4**, e06262 (2015).
32. Jörntell, H. Cerebellar physiology: links between microcircuitry properties and sensorimotor functions. *J. Physiol. (Lond.)* **595**, 11–27 (2017).
33. Medina, J.F. & Lisberger, S.G. Variation, signal, and noise in cerebellar sensory-motor processing for smooth-pursuit eye movements. *J. Neurosci.* **27**, 6832–6842 (2007).
34. ten Brinke, M.M. *et al.* Evolving models of Pavlovian conditioning: cerebellar cortical dynamics in awake behaving mice. *Cell Rep.* **13**, 1977–1988 (2015).
35. Lisberger, S.G. & Medina, J.F. How and why neural and motor variation are related. *Curr. Opin. Neurobiol.* **33**, 110–116 (2015).
36. Jirenhed, D.-A. & Hesslow, G. Are Purkinje cell pauses drivers of classically conditioned blink responses? *Cerebellum* **15**, 526–534 (2016).
37. Lee, K.H. *et al.* Circuit mechanisms underlying motor memory formation in the cerebellum. *Neuron* **86**, 529–540 (2015).
38. Billings, G., Piasini, E., Lőrincz, A., Nusser, Z. & Silver, R.A. Network structure within the cerebellar input layer enables lossless sparse encoding. *Neuron* **83**, 960–974 (2014).

ONLINE METHODS

Animal preparation for *in vivo* two-photon calcium imaging. Experimental procedures were approved by the Princeton University Institutional Animal Care and Use Committee and performed in accordance with the animal welfare guidelines of the National Institutes of Health. Details of animal preparation were modified from previously published procedures²⁴. For imaging experiments we used 5 male, 12- to 16-week-old C57BL/6J mice (Jackson Laboratory) and 2 male, 20-week-old B6.Cg-Tg.NeuroD1-Cre.GN135Gsat mice. All mice were group-housed on a reversed light cycle. During the surgery mice were anesthetized with isoflurane (5% for induction, 1.0–2.5% for maintenance) and a 3-mm-wide craniotomy was opened. A custom-made two-piece headplate²⁴, with a removable part to allow repeated access for viral injections, was attached to the animal's head. To increase stability, the skull was thoroughly cleaned in the region surrounding the target imaging zone (lobule VI of the cerebellar vermis) and except for the craniotomy zone, the skull surface was covered with Metabond (Parkell, S380) before opening a craniotomy. For imaging experiments, after an overnight delay for animal recovery, the top plate was removed for delivery of 400–800 nL (~50 nL/min) of virus (for C57BL/6J mice, AAV1.Syn.GCaMP6f.WPRE.SV40 virus (Penn Vector Core, lot AV-1-PV2822) or AAV1.Syn.GCaMP6f-RS09.WPRE.SV40; for NeuroD1-cre mice, AAV1.CAG.Flex.GCaMP6f.WPRE.SV40) in two injections ~750 and ~1,250 μ m lateral to the midline and 250 μ m deep from the dura surface using borosilicate glass pipettes (World Precision Instruments, 1B100F-4, 1/0.58 mm OD/ID) beveled to 30 degrees with a 10- to 20- μ m tip opening. In two mice (one hSyn, one NeuroD1-cre), craniotomies and injections were performed during the same surgery, an imaging window was implanted and glued onto the skull, and a standard aluminum headplate was cemented to the skull for the purpose of head fixation. All animals were placed back in their home cage for 2 weeks of recovery.

Habituation and eyeblink training for chronic experiments. Two to 3 weeks after AAV injections, animals were trained as previously described⁸. Animals were first habituated to a freely-rotating treadmill for repeated intervals over at least 5 d of graded exposure. After habituation was complete, animals were trained while simultaneously measuring brain activity under a two-photon microscope. To minimize the learning time, animals were trained for up to 4 short sessions per d. The number and duration of training sessions were varied according to the type of CS and the behavioral state of the animal. If an animal showed signs of discomfort, it was returned to its home cage for up to 24 h. The US was a periorbital airpuff (10–20 psi, 30 ms in duration, delivered via a plastic needle placed 5 mm from the cornea and pointed at it). The conditional stimulus was a flash of light (400 nm, 'light CS', 500 ms, contralateral to the US) or an airpuff to whisker vibrissae (2–3 psi, 'whisker CS', 800 ms, ipsilateral to the US). Consistent with other recent eyeblink conditioning in mice^{8,34}, the CS and US did not coterminate, which allows the CS–US interval to be varied without changing the CS duration. In experiments using light CS, the CS–US interval was 250 ms from CS start to US start, and training spanned 7–12 d. In experiments using whisker CS, the CS–US interval was 440 ms since vibrissa stimulation allowed for larger interstimulus intervals; learning was faster⁸ and training spanned 6 d. For randomization purposes, the stimuli were randomly presented, with a proportion 80% CS + US, 10% CS alone and 10% US alone.

Identification of imaging zone. At the beginning of the first day of measurements, a CS-responsive cerebellar zone was identified by delivering 10 CS–US paired stimuli while imaging zones in the vermis of lobule VI, between the midline and the paravermal vein. The average fluorescence response to the CS in the zone was computed during the experiment using a custom ImageJ (<http://imagej.nih.gov>) macro, and zones showing >20% $\Delta F/F$ were selected for further imaging. CS–US pairings were used to prevent delays in learning that can arise from latent inhibition caused by nonreinforced pre-exposure to the CS³⁹. For later recording sessions, the FOV was matched first using surface landmarks such as blood vessels, then using the brain surface overlying the imaging zone for further localization and finally by comparing the fluorescent FOV itself with previous sessions.

Data acquisition. Behavioral data was collected using custom software in Python (<https://www.python.org/>). In the first set of experiments, imaging data was collected using ScanImage version 3.8.1 (Vidrio Technologies). Behavioral

acquisition software on one computer sent triggering signals to drive a National Instruments USB card (PCIe 6363) on a second computer for image acquisition. Calcium imaging was acquired at 128 \times 64 pixels per frame at 15.6 Hz or 128 \times 128 at 3.9 Hz (64 or 256 ms per frame, 1 ms per line, bidirectional scanning), and behavioral data was acquired in 320 \times 240-pixel movies at 100 Hz (Sony PS3 Eye, interfaced with custom software written in Python). Imaging and behavioral data were collected in 4-s epochs per trial. Within each trial, the CS stimulus was delivered 1.92 s (baseline activity) after the starting trigger. To synchronize data, ScanImage channel 2 was used to record the eyelid signal output from the Python module and channel 3 was used to record CS, CS–US and US triggers.

In the second set of experiments, imaging data was collected using ScanImage 2015 (Vidrio Technologies). Behavioral acquisition software on one computer sent triggering and synchronization signals via a National Instruments card (USB 8451) to a second computer for image acquisition. Calcium imaging was acquired at 512 \times 512 pixels per frame at 29 Hz and behavioral data in 320 \times 240-pixel movies at 60 Hz (Sony PS3 Eye, interfaced with custom software written in Python). Data were collected in 8-s epochs. Within each trial, the CS stimulus was delivered 4 s after the starting trigger. To synchronize data, an I2C-based synchronization protocol was used to send trial timing information from the behavior acquisition computer to the imaging computer in real time.

The number of trials per session depended on the animal stress level and ranged from 25 to 100 trials. Eyelid position was extracted from the movies collected with the PS3 camera. During training, eyelid closure was measured as the integral of a manually defined zone enclosing the eye. Animal self-motion and locomotion were estimated from camera images through a custom-built image processing pipeline (see "Behavioral tracking" section, below). Each trial was initiated only if the animal was still, the eyelid was open and an interval of at least 12 s had elapsed from the previous trial. Thresholds for eyelid closure and movement were set from baseline signals at the time of the experiment. In the figures, example data came from mice using the two expression strategies as follows: NeuroD1-cre (Figs. 1c–e, 5a,d,e and 6b; **Supplementary Videos 1 and 2** and **Supplementary Figs. 1a,b and 8a–c,d**) and AAV1-hSyn (Figs. 1b, 3, 4a,b,d, 5b,c,e and 6a,b and **Supplementary Figs. 1b, 2, 3, 6 and 8b,c,d**).

Channelrhodopsin-2 stimulation. B6.Cg-Tg(Thy1-COP4/EYFP)18Gfng/J mice (Jackson Laboratories, 007612) expressing channelrhodopsin-2 within the cerebellum exclusively in mossy fibers⁴⁰ (**Supplementary Fig. 4**) under the Thy-1 promoter were implanted with an optical window as described above. After 1 week of recovery, they were habituated to the treadmill. Using an Olympus 4 \times macro objective (NA = 0.28 and WD = 29.5 mm) light from a blue LED (470 nm, LUXEON Rebel, #SP-03-B4) was focused ~200–400 μ m under the cerebellum surface (125–250 mW/mm²). Ten to 50 stimuli of 10 ms duration and 50 Hz frequency were delivered at different locations (crus I and II; lobules V, VI and simplex) of cerebellar surface. Movements were extracted as the frame-on-frame value among manually selected motion components and calculated as the squared interframe pixel difference averaged across manually selected regions of interest (limbs, whiskers, oral trunk–neck) from high-speed infrared movies. The resulting traces were averaged after aligning to the light pulse triggers and removing the prestimulus baseline.

Offline analysis of blinks. CR⁺ (or CR[−]) trials were identified as responses greater (or smaller) than 10% of the full blink in a window from 50 ms before to 30 ms after the US trigger. Trials with only US presentation or CS presentation were termed US-alone and CS-alone trials.

Behavioral tracking. To isolate the effect of unrelated self-motion and/or proprioceptive sensory activity, we developed an image processing pipeline to extract quantitative measures of motor behaviors from videos recorded through a high-frame-rate camera positioned in front of (but not orthogonal to) the animal. As a proxy for locomotion, wheel velocity was estimated through a model-based approach to tracking wheel motion. First, a model of the wheel was constructed by measuring the physical dimensions of the uniformly spaced bumps (nubs) on the wheel surface. A simplified representation of the wheel (**Supplementary Fig. 7** and **Supplementary Video 3**) was then manually registered to the surface of a minimally occluded region of the wheel. This enabled the calculation of a projective transformation matrix that corrected for the perspective distortion introduced by the nonorthogonal positioning of the behavior camera. The reprojected

videos were contrast-normalized via CLAHE⁴¹ and an ROI was selected such that there was again minimal occlusion from the animal's body. Next, HOG features⁴² centered at each pixel in the ROI were extracted as a way to describe the appearance of the local image region. This proved robust to differences in illumination artifacts and particularly to heterogeneity in the wheel's texture. Extracted features were matched across subsequent frames by finding the nearest neighbor with a ratio of its Euclidean distance to that of the next nearest neighbor of at least 0.7. This matching procedure reduced the rate of ambiguous matches by ensuring they were sufficiently distinct but did not guarantee that there would be matches between frames; for these, linear interpolation was used to fill in missing data. Finally, the wheel velocity was estimated from the median displacement in the ROI converted to physical units by scaling to the wheel model.

To measure self-motion in the form of movement of snout and whisker muscles in the absence of locomotion or wheel displacement, we devised a method for tracking a set of manually selected seed points along the contour of the animal's snout with the assumption that most self-motion would result in changes in its shape (Supplementary Fig. 7 and Supplementary Video 4). The snout was automatically segmented from the background using Otsu's method⁴³ to find an optimal threshold for separating distributions in the image intensity histograms. The points along the boundary of the mask were then used as candidate points for matching to the original seed points that traced the contour of the snout. As these motions were highly nonlinear and segmentation did not always result in perfect separation from the background, matching was achieved via coherent point drift⁴⁴, a robust point set registration algorithm. Matching was performed across frames by selecting the closest contour-line point subject to rigidity constraints in deformation of the seed contour. The contour line traces were then used as trajectories of the snout shape used to estimate displacements in pixels per s. As imaging conditions varied greatly across videos, a secondary pipeline was developed to process videos that could not be tracked using the aforementioned method. For these cases, an ROI was selected such that only the upper part of the snout of the animal and no wheel pixels were included. This region was tiled into evenly spaced blocks (12 × 12 pixels) and matched across frames via normalized cross-correlation, i.e., block matching. Tracking the trajectories of each block enabled results comparable to those returned by the shape-based approach but may not have included subtle motions of the tip of the snout.

Calcium imaging data analysis. Image data analysis was performed using custom Matlab, Python and ImageJ scripts. Movies were processed in batches containing a maximum of 18,000 frames per batch and were fragmented when changes in FOVs were too dramatic. As a first step, movies were motion-corrected using the 'template matching and slice alignment' ImageJ plugin (<https://sites.google.com/site/qingzongtseng/template-matching-ij-plugin>), which is based on the 'opencv' matching template function, or using an equivalent Python implementation (<https://github.com/simonsfoundation/CalmAn>) for the second set of experiments. For slow scan (i.e., <25 Hz), in order to compensate for warping induced by brain movement and scanning microscopy, we separately corrected the top and bottom portions of each movie for motion and then stitched them back together. For the first batch of experiments, before matrix factorization, movies were preprocessed to set a baseline of 0 and a range of 0–1. Slow changes in the pixel fluorescence time series were removed by examining the distribution of fluorescence in a ± 5 -s interval around each sample time point and subtracting the 8th percentile value¹⁶. Finally, the movies were normalized to a range of 0–1. For the second batch, we used an updated version of CNMF that did not suffer from arbitrary signal scale or baseline.

For ROI identification, we used a Python package (<https://github.com/simonsfoundation/CalmAn>) for calcium image source separation based on non-negative matrix factorization (NMF)²⁶. The algorithm is specialized for separating signals from overlapping structures by relying on the fact that signals from different structures often have different time signatures. This algorithm allowed removal of activity from diffuse sources, a pattern consistent with ascending axons passing through neuropil (Supplementary Video 2). The resulting estimate of neuropil activity was removed from the movie, and a subset of the ROIs was selected that corresponded to GrCs. The neuropil-subtracted movie was renormalized to F values, and traces were extracted using the selected regions of interest. $\Delta F/F_0$ was computed as previously¹⁶ except using baseline (F_0) values extracted using NMF. In slow-scanning experiments, temporal precision was corrected using the relationship between scanning position and time to remap each FOV to true time within

the frame. When possible, neurons were matched across days or sessions ($n = 3$ mice). To match neurons across days, we wrote a special purpose script to align FOVs from different days using the opencv 'template matching' function and then matched the regions by maximizing an intersection over union metric (cells were matched when the ratio of overlapping pixels vs. total pixels was maximal). Imaging and behavioral data were synchronized by resampling both signals to 30 Hz and aligning them based on the eyelid and trigger signals. Cells of the same identity were confirmed by exact location across days in three animals, and aggregated population analysis was done in three animals whose FOV changed slightly over multiple days ($n = 2$) or were imaged only after training ($n = 1$). The criteria for selecting GrCs were based on size (4.5–7.5 μm), location within the brain (under the Purkinje cell layer) and range of activity (max range, 400% $\Delta F/F_0$). In the first batch, GrCs were selected manually from the extracted components ($n = 4$ mice) and in the second were selected in a fully automatic manner ($n = 2$ mice). The selection of GrCs did not depend on the experimental conditions but was the automatic/semimanual result of the CNMF algorithm plus selection criteria from histology (see "Histological procedures" section, below).

$\Delta F/F_0$ traces were aligned to the delivery of stimuli (0 s being the time of expected US), and the median value during baseline (1 s preceding CS or US stimulus delivery) was subtracted from the waveform.

Correlation computation. In order to quantify the similarity between GrC activities and behavioral responses, we first aligned and binned in 100 ms bins behavior and fluorescence. Then, correlation between neural activity and snout or wheel dynamics was quantified with the Pearson's r coefficient between neural activity and GrC activity excluding the window of stimulus delivery (between 500 ms before and 1,500 ms after the US). In order to compute the regressor between neural activity and conditional or unconditional responses, the same correlation above was calculated during the stimulus delivery time: 500 ms before to 35 ms after US for CR correlation and from 35 before to 750 ms after the US for UR. To estimate the confidence interval for correlation, we repeated the procedure described after first shuffling the trials and then taking the 95th percentile of the distribution as the threshold.

Multivariate linear regression. In order to probe the redundancy in the population code, we implemented a multivariate linear regressor that was trained using half of the trials randomly selected and evaluated on the remaining half. The regressor was implemented by the scikit sklearn.linear_model.LinearRegression (http://scikit-learn.org/stable/modules/generated/sklearn.linear_model.LinearRegression.html). This corresponds to the regression of an n -dimensional response on a matrix of predictor variables, with normally distributed, potentially heteroscedastic and/or correlated errors. The regressor was run 100 times on different random subdivisions of trials (50% training and test sets), giving rise to a distribution of solutions. The fitness of each solution was quantified by computing the correlation coefficient between the predicted and actual values of the eyelid magnitude (e^*) in test trials (Fig. 4c). To test the redundancies of the neural code, we trained it on smaller subsets of neurons to assess the performance degradation (Fig. 4d) and compared its performance to the highest-correlation cell in the remaining subpopulation (Fig. 4d).

Redundancy calculation. Redundancy was quantified by dividing the maximum possible amount of Shannon information present in GrC population activity by the actual amount of information found in GrC-based predictions of CR amplitude. The mutual information, M , between the regressor (or a single-neuron signal) prediction and eyeblink output amplitudes was calculated as $M = -1/2 \log_2(1 - r^2)$, where r is the Pearson correlation coefficient between the predicted and actual eyeblink amplitude, calculated on a trial-by-trial basis. This expression is equivalent to $M = 1/2 \log_2(v/v_\delta)$, where v is the variance in eyelid position across trials and v_δ is the residual variance that is unexplained by the regressor or single-neuron signal. The redundancy was calculated as $\Lambda = \Sigma M_i / M_{\text{regressor}}$, where the summation occurs across all individual neurons, i .

Statistics. Most of the statistics and grouping were performed using Python pandas (<http://pandas.pydata.org/>). Values in text are reported as mean \pm s.d. unless otherwise indicated. When reported, P -values are calculated employing two-tailed unpaired or paired t -tests. Regarding the assumption of normality, amplitudes and granule-cell fluorescence signals appeared bimodal when pooled

across all trials and unimodal when sorted into responding (CR⁺) and nonresponding (CR⁻) trials. Therefore, sorted trials were used for statistical analysis. All the statistics on neural activity or behavior were calculated only if at least ten cells or at least eight trials were available per FOV or session, excepting UR-related computation, for which the number was lowered to four trials. Because we imaged anywhere from 30 to 400 GrCs per mouse, to obtain a uniformly distributed sample across mice (Fig. 5e and Supplementary Fig. 8c), bootstrapping was done with 30 GrCs per animal. No statistical methods were used to predetermine sample sizes, but our sample sizes are similar to those reported in previous publications⁴⁵. We also report the computed power of the study in the **Supplementary Methods Checklist**.

Histological procedures. Mice were anesthetized with pentobarbital and perfused with 4% paraformaldehyde. Brains were isolated and processed as previously described^{46,47}. Following perfusion, brains were incubated in 10% sucrose, embedded in gelatin, rapidly frozen, sectioned coronally at 40 μ m and collected in 0.1 M PBS. Sections were processed for immunohistochemistry by washing with PBS and incubation in a blocking buffer (10% normal horse serum, 0.5% Triton X-100 in PBS) before a 3-d incubation at 4 °C in PBS buffer containing 2% NHS, 0.4% Triton X-100 and the following primary antibodies: brains from mice used in the cerebellar-inactivation/muscimol study ($n = 5$) were stained for zebrin bands using goat anti-aldolase-C antibody (sc-12065; Santa Cruz Biotechnology, 1:1,000, previously described in Zhou *et al.*⁴⁸); brains from mice used for GrC identification and counts were stained with rabbit anti-GABA_A $\alpha 6$ receptor antibody (G0295; Sigma, 1:1,000, previously described in Jaarsma *et al.*⁴⁷; $n = 4$ mice; two C57BL/6J injected with AAV1.Syn.GCaMP6f.WPRE.SV40 virus and two B6.Cg-Tg.NeuroD1-Cre.GN135Gsat mice injected with AAV1.CAG.Flex.GCaMP6f.WPRE.SV40). Viral injections and surgeries were performed as described above. One of the NeuroD1-cre mice used for histological studies was first used for *in vivo* calcium imaging experiments (Fig. 1e). Next, sections were washed in PBS, incubated for 2 h at room temperature (20–22 °C) in PBS buffer with secondary antibodies, counter stained with DAPI for 10 min (30 μ l/mL) and mounted on glass slides with Vectashield antifade mounting medium (H-1000; Vector Laboratories, USA). Alexa Fluor 488-conjugated donkey anti-goat secondary antibody was used to visualize aldolase C immunoreactivity (Jackson ImmunoResearch, West Grove, PA; Invitrogen; 1:200) and Alexa Fluor 633-conjugated goat anti-rabbit secondary antibody (Jackson ImmunoResearch, West Grove, PA; Invitrogen; 1:200) was used on brains incubated with rabbit anti-GABA_A $\alpha 6$ receptor primary antibody. Sections stained for immunofluorescence were scanned with a Leica SP8 confocal laser-scanning microscope (Leica Microsystems, Germany) using 10 \times , 40 \times and 63 \times objectives, hybrid (HyD) detectors for sensitive detection and sequential scan mode. To visualize expression of channelrhodopsin-2 in B6.Cg-Tg(Thy1-COP4/EYFP)18Gfng/J cerebellar tissue was cleared using passive clearing with CLARITY⁴⁹ and imaged on a two-photon microscope under a 10 \times objective.

Characterization and quantification of GCaMP-positive cells. Cerebella of hSyn and NeuroD1-cre animals were sectioned coronally at 40 μ m, processed for immunofluorescence staining of the GABA_A $\alpha 6$ receptor and counterstained with DAPI as described above. All quantifications were performed manually in randomly selected FOVs of 10⁴ μ m² using the ImageJ plugin Cell Counter. For each section, DAPI-positive cells were counted and scored for the expression of GCaMP and costaining of GABA_A $\alpha 6$ receptors. Next, GCaMP-positive structures with cell-like characteristics (round shape, > 4.5 μ m) but without DAPI counterstaining were scored and analyzed for costaining of GABA_A $\alpha 6$ receptors. For quantification, cells were subdivided into two groups according to size, 4.5–7.5 μ m and >7.5 μ m, and further characterized as follows: (i) GrCs: GABA_A $\alpha 6$ receptor-positive, DAPI positive and 4.5–7.5 μ m in size; (ii) non-GrCs: DAPI-positive, GCaMP-positive structures >7.5 μ m; and (iii) 'potential' GrCs: GCaMP-positive, DAPI-negative structures of 4.5–7.5 μ m in size. Because of the limited number of large cells, to get a better estimate of cells >7.5 μ m, we included counts of complete lobules (tile scan; $\sim 25\times$ bigger FOV) and normalized the counts to a FOV of 10⁴ μ m². All cell count analysis was performed blind with respect to the genotype of the animal.

Acute brain slice experiments. Mossy fiber stimulation recordings and calcium imaging of GrCs: seven male, 6-week-old C57BL/6J mice were anesthetized with

isoflurane and injected in lobule VIb with AAV1.Syn.GCaMP6f.WPRE.SV40 virus as described in the "Animal preparation" section, above. Four to 5 weeks later, 250- μ m-thick sagittal cerebellar brain slices were prepared using ceramic blades (Lafayette Instrument Co., Lafayette, IN) on a vibratome (VT1000S, Leica, Germany) set to speed 1.0–2.5 and frequency 8–9 under immersion in oxygenated, ice-cold (~ 4 °C) artificial CSF (aCSF) containing (in mM) 126 NaCl, 3 KCl, 1 NaH₂PO₄, 20 D-glucose, 25 NaHCO₃, 2 CaCl₂ and 1 MgCl₂. Brain slices were preincubated at 34 °C for 40–60 min, then kept at room temperature. For recording, slices were transferred to an immersion-type recording chamber perfused at 2–4 mL/min with oxygenated aCSF at ~ 34 °C. For extracellular mossy fiber stimulation, a large patch electrode filled with aCSF was positioned at the surface of the slice. GrCs were imaged using a custom-built two-photon laser scanning microscope using pulsed 900-nm excitation from a Ti:sapphire laser (Mira 900, Coherent). Excitation power was kept below 15 mW at the backplane of the objective (40 \times , NA 0.8, IR-Achroplan; Carl Zeiss, Thornwood, NY). Data acquisition was controlled by ScanImage v 3.6.1 (Vidrio Technologies).

Loose patch recordings/stimulation and calcium imaging of GrCs: eight male mice were used. Unless reported, animal and slice preparation was done as described above. Cerebella were removed and dissected in ice-cold oxygenated slicing medium containing (in mM): 93 N-methyl-D-glucamine, 93 HCl, 2.5 KCl, 5 sodium ascorbate, 2 thiourea, 3 sodium pyruvate, 0.5 CaCl₂, 10 MgCl₂, 30 NaHCO₃, 1.2 NaH₂PO₄, 20 HEPES and 25 D-glucose (mOsm 300, pH 7.4). We cut 250- μ m sagittal slices of the vermis on a vibratome (VT2000S, Leica, Germany). Slices were incubated in slicing medium at near-physiological temperature (34 °C) for 2 min and transferred to 34 °C aCSF for 30 min. Subsequently, slices were held in a chamber filled with oxygenated aCSF at room temperature, covered with aluminum foil to prevent too much light exposure and used within 6 h. Experiments were performed in aCSF at near-physiological temperature (~ 33 °C). Loose cell-attached recordings were performed under a multiphoton microscope (A1R MP+, Nikon, Japan) and Axon Multiclamp 700A amplifier. The patch pipettes (7–9 M Ω) were filled with intracellular solution containing (in mM): 120 potassium-glucuronate, 9 KCl, 10 KOH, 3.48 MgCl₂, 4 NaCl, 10 HEPES, 4 Na₂ATP, 0.4 Na₃GTP, 17.5 sucrose and 10–20 μ M Alexa Fluor 594 (at pH 7.25). To reliably elicit action potential firing in granule and Golgi cells, 100–200 mV of voltage steps lasting 1 ms were delivered through the patch pipettes. Imaging data was collected using NIS-Elements software (Nikon Instruments). Signals were synchronized using imaging software as an external trigger for the Axon Multiclamp 700A amplifier. Calcium imaging was acquired at 30 Hz (1 ms per line, bidirectional scanning).

Cerebellar inactivation experiments. Five male C57BL/6J mice were equipped with a 3-mm-wide cranial window covered by a silicone plug (Kwik-Sil, WPI) and a custom-made two-piece headplate (see "Animal preparation" section, above, for details). Following a 3-d recovery period, mice were habituated and trained in the custom-built eyeblink setup described earlier^{34,50}. Mice were habituated for 5 d and then trained for up to 1 h/d for a period of 11 d.

The US and CS were delivered as described above. For CS, a flash of light (400 nm, 500 ms, contralateral to the US) was used for all conditional mice. On average, mice received 220 trials per d (200 CS–US paired trials and 20 CS-only probe trials). For randomization purposes, the stimuli were randomly presented, with 80% CS + US, 10% CS alone, 10% US alone. After 11 d of training, all mice reached stable performance levels (CR production $\sim 80\%$). On day 12, the first inactivation experiment was performed. Mice first received 110 baseline trials (100 CS–US paired trials and 10 CS-only trials), and then they were taken out of the setup, lightly anesthetized with isoflurane and fixed in a stereotactic frame. The silicone plug was removed and 100-nL injections of either 0.5% muscimol (Tocris with 1% Evans Blue) dissolved in sterile saline (0.9% NaCl, Hospira) or the vehicle (saline) were given at the same coordinates used for imaging neural responses. In order to reach the GrC layer and ensure the reproducibility of the injection size, injections were made ~ 300 μ m deep from the surface of the brain using a Nanoject II Auto-Nanoliter Injector (Drummond Scientific Company, USA). After injections, the brain was covered with the plug, mice were placed back in the setup, and after 15 min recovery time, they were subjected to 110 eyeblink conditioning trials (100 CS–US paired trials and 10 CS-only trials). The next day (day 13) the inactivation experiment was repeated but the drug/vehicle condition was switched, meaning that mice that had received saline on day 12 were injected with 0.5% muscimol, and mice that had been injected with the drug received the vehicle. Immediately

after acquiring the postinjection trials, an overdose of sodium pentobarbital (0.15 mL i.p.) was administered allowing transcardial perfusion (0.9% NaCl followed by 4% paraformaldehyde in 0.1 M phosphate buffer (PB); pH = 7.4) to preserve the tissue for histological verification of the injections. Data analysis was performed blind to the conditions of the experiments.

Data availability statement. The data that support the findings of this study are available from the corresponding author upon reasonable request. The code for calcium analysis is available for download from <https://github.com/simonsfoundation/CalmAn> (release 0.5, El Cocodrilo).

39. Lubow, R.E. Latent inhibition. *Psychol. Bull.* **79**, 398–407 (1973).

40. Wang, H. *et al.* High-speed mapping of synaptic connectivity using photostimulation in channelrhodopsin-2 transgenic mice. *Proc. Natl. Acad. Sci. USA* **104**, 8143–8148 (2007).

41. Zuiderveld, K. Contrast limited adaptive histogram equalization. in *Graphics Gems IV* (ed., Heckbert, P.S.) 474–485 (Academic Press Professional, Inc., 1994).

42. Dalal, N. & Triggs, B. Histograms of oriented gradients for human detection. *IEEE Computer Society Conference on Computer Vision and Pattern Recognition*. 886–893 (2005).

43. Otsu, N. A threshold selection method from gray-level histograms. *IEEE Trans. Syst. Man Cybern.* **9**, 62–66 (1979).

44. Myronenko, A. & Song, X. Point set registration: coherent point drift. *IEEE Trans. Pattern Anal. Mach. Intell.* **32**, 2262–2275 (2010).

45. Huber, D. *et al.* Multiple dynamic representations in the motor cortex during sensorimotor learning. *Nature* **484**, 473–478 (2012).

46. Badura, A. *et al.* Climbing fiber input shapes reciprocity of Purkinje cell firing. *Neuron* **78**, 700–713 (2013).

47. Jaarsma, D. *et al.* A role for bicaudal-D2 in radial cerebellar granule cell migration. *Nat. Commun.* **5**, 3411 (2014).

48. Zhou, H. *et al.* Cerebellar modules operate at different frequencies. *Elife* **3**, e02536 (2014).

49. Chung, K. & Deisseroth, K. CLARITY for mapping the nervous system. *Nat. Methods* **10**, 508–513 (2013).

50. Kloth, A.D. *et al.* Cerebellar associative sensory learning defects in five mouse autism models. *Elife* **4**, e06085 (2015).